



LAWRENCE
LIVERMORE
NATIONAL
LABORATORY

X-ray Spectral Measurements and Collisional Radiative Modeling of Hot, Gold Plasmas at the Omega Laser

M. J. May, M. B. Schneider, S. B. Hansen, H.-K. Chung, D. E. Hinkel, H. A. Baldis, C. Constantin

July 8, 2008

High Energy Density Physics

Disclaimer

This document was prepared as an account of work sponsored by an agency of the United States government. Neither the United States government nor Lawrence Livermore National Security, LLC, nor any of their employees makes any warranty, expressed or implied, or assumes any legal liability or responsibility for the accuracy, completeness, or usefulness of any information, apparatus, product, or process disclosed, or represents that its use would not infringe privately owned rights. Reference herein to any specific commercial product, process, or service by trade name, trademark, manufacturer, or otherwise does not necessarily constitute or imply its endorsement, recommendation, or favoring by the United States government or Lawrence Livermore National Security, LLC. The views and opinions of authors expressed herein do not necessarily state or reflect those of the United States government or Lawrence Livermore National Security, LLC, and shall not be used for advertising or product endorsement purposes.

X-ray Spectral Measurements and Collisional Radiative Modeling of Hot, Gold Plasmas at the Omega Laser

M.J. May, M.B. Schneider, S.B. Hansen, H.-K. Chung, D.E. Hinkel^a
H.A. Baldis^b C. Constantin^{b,c}

^a*PO Box 808, L281, Lawrence Livermore National Laboratory, Livermore CA 94551.*

^b*University of California at Davis, One Shields Avenue, Davis, California 95616*

^c*now at University of California at Los Angeles, 405 Hilgard Avenue, Los Angeles, California 90024*

Abstract

M-Band and L-Band Gold spectra between 3 to 5 keV and 8 to 13 keV, respectively, have been recorded by a photometrically calibrated crystal spectrometer. The spectra were emitted from the plasma in the laser deposition region of a 'hot hohlraum'. This is a reduced-scale hohlraum heated with ≈ 9 kJ of 351 nm light in a 1 ns square pulse at the OMEGA laser. The space- and time- integrated spectra included L-Band line emission from Co-like to Ne-like gold. The three L-Band line features were identified to be the $3s \rightarrow 2p$, $3d_{5/2} \rightarrow 2p_{3/2}$ and $3d_{3/2} \rightarrow 2p_{1/2}$ transitions at ≈ 9 keV, ≈ 10 keV and ≈ 13 keV, respectively. M-Band $5f \rightarrow 3d$, $4d \rightarrow 3p$, and $4p \rightarrow 3s$ transition features from Fe-like to P-like gold were also recorded between 3 to 5 keV. Modeling from the radiation-hydrodynamics code LASNEX, the collisional-radiative codes FLYCHK and SCRAM, and the atomic structure code FAC were used to model the plasma and generate simulated spectra for comparison with the recorded spectra. Through these comparisons, we have determined the average electron temperature of the emitting plasma to be between 6.0 and 6.5 keV. The electron temperatures predicted by LASNEX appear to be too large by a factor of about 1.5.

Key words:

52.20.Fs, 52.25.Jm, 34.70.+e, 34.30.lj

1 Introduction

Reduced-scale hohlraums heated by high power lasers are being developed as x-ray sources for studies of materials under extreme conditions [1–3]. Depositing a large amount of laser energy (~ 10 kJ) into a small cylindrical gold hohlraum on nanosecond time scales produces a hot radiation environment inside the hohlraum. The achieved radiation temperatures are ~ 300 eV. As they are heated, the gold material in the hohlraum walls is ablated, quickly filling the hohlraum with high-Z plasma. The electrons in this plasma, heated mainly through inverse bremsstrahlung interactions with the laser, conduct heat to the hohlraum walls. The walls absorb and re-emit the heat through x-rays, producing the high thermal radiation field. The plasma also interacts with the drive laser through laser-plasma interactions (LPI). The LPI are dependent on the plasma parameters (e.g. electron temperature, electron density, plasma flow, charge state, etc.) and include parametric instabilities (e.g. stimulated Raman backscatter (SRBS), stimulated Brillouin backscatter (SBBS)) [4], filamentation, crossed-beam energy transfer, and beam deflection [5]. The extreme plasma conditions in reduced-scale hohlraums may also give rise to novel LPI mechanisms, such as rescatter (SBBS of stimulated Raman forward scatter) [6]. An additional instability, the two-plasmon decay (TPD), can promote absorption of laser irradiation at quarter critical density and the generation of super-thermal electrons. The experiments in this paper are above the laser power threshold for TPD. This instability has been observed in a variety of OMEGA experiments [7]. Since LPI instabilities can reduce laser-hohlraum coupling [5] and thus reduce the thermal radiation field, LPI losses must be understood and then mitigated for successful use of reduced-scale hohlraums as backlighters or thermal radiation drivers for materials studies or inertial confinement fusion studies (ICF). A better understanding of the hohlraum plasma and LPI can be obtained by comparing the measured plasma parameters (electron temperature, electron density, ionization state, etc.) to radiation-hydrodynamic simulations.

A common method for determining plasma parameters is through analysis of spectroscopic measurements. Particular emission lines and features in a recorded spectrum can be identified as belonging to particular charge states. By comparing modeled emission spectra from a range of ions to the measured emission features, one can infer an experimental charge state distribution (CSD). This can then be compared with temperature-dependent CSD predictions from collisional-radiative models to estimate the plasma temperature. This type of CSD analysis have been performed by several authors. On the Nova laser [8], Foord *et al.* [9] buried a gold microdot in a Be foil that was laser heated to steady state conditions with electron temperature, $T_e = 2.2$ keV (determined from Thomson scattering measurements) and $n_e = 6 \times 10^{20}$ cm $^{-3}$ (measured by imaging the target expansion). In these conditions, the

5f→3d lines in the 3 to 4 keV photon energy range from Ni-like to As-like gold ions were used to infer an average charge state $\langle q \rangle$ of 49.3 by comparing the recorded spectrum with modeling from the Hebrew University Lawrence Livermore Atomic Code (HULLAC) [10]. In other work, Glenzer *et al.* [11] created and characterized a fusion hohlraum plasma with $T_e = 2.6$ keV, $n_e = 1.4 \times 10^{21} \text{ cm}^{-3}$ and $T_{rad} = 210$ eV. The measured spectrum of the 5f→3d lines were used to infer a $\langle q \rangle$ of 52 ± 1 . The inferred CSDs from both of these experiments were in reasonable agreement with predictions from the plasma modeling code RIGEL [12]. Recently at the OMEGA Laser facility [13], Heeter *et al.* [14,15] determined the ionization balance of well characterized Non-Local Thermal Equilibrium (NLTE) gold plasmas with and without external radiation fields at electron densities near 10^{21} cm^{-3} and various electron temperatures spanning the range 0.8 to 2.4 keV. Time- and space-resolved M-shell gold emission spectra were analyzed using a collisional-radiative model with hybrid level structure [16], finding average charge states $\langle q \rangle$ ranging from 42 to 50. At the lower temperatures (~ 165 eV), the spectra included emission features from complex N-shell ions and exhibited significant sensitivity to external radiation fields.

The determination of the CSD is also important for other low-Z to high Z element NLTE plasmas. For instance, C. Chenais-Popovics *et al.* [17] benchmarked the ionization balance of Xe through x-ray M-shell spectroscopy of a laser-produced gas jet xenon plasma. Thomson scattering was used to measure the electron temperature and density. A comparison of the experimental x-ray spectra with calculations performed ab initio with a NLTE collisional-radiative model based on the superconfiguration formalism yielded good agreement. A more extensive investigation of the ionization balance for multiple elements is done by the NLTE Code Comparison Workshops [18–21]. At the last workshop [21] detailed comparisons were done between the calculated CSD of various atomic codes for several elements (e.g. C, Ar, Fe, Sn, Xe and Au). The agreement among NLTE codes has improved significantly over the last decade due in part to benchmark measurements [9,11,22] and in part to advances in modeling theory arising from detailed comparisons of different model assumptions in the NLTE workshops. This improvement can be seen in the calculations for Au. In the first workshop, the predicted average charge state, $\langle q \rangle$, for gold at a temperature, T_e , of 2.5 keV and a density, n_e , of 10^{20} cm^{-3} varied from +43 to +63! In the fourth workshop, the predicted charge state of Au at the same conditions was ~ 47 with a variation of roughly ± 5 . However, some of the other plasma conditions exhibit a larger spread. The experiments presented here can be used to guide and improve the calculation further.

For the higher electron temperatures that exist in the plasma in the reduced-scale hohlraums, it is necessary to measure higher charge states of gold at higher photon energies. Here, we present analyses from both M-band and L-band spectra recorded from reduced-scale hohlraum plasmas in NLTE condi-

tions produced with the OMEGA laser. We observed the $3s \rightarrow 2p$, $3d_{3/2} \rightarrow 2p_{1/2}$ and $3d_{5/2} \rightarrow 2p_{3/2}$ L-Band transitions between 8 to 13 keV and the $5f \rightarrow 3d$ M-Band transitions between 3 to 5 keV from Co-like to Ne-like gold ions. The HENWAY [23] x-ray crystal spectrometer was used to record the gold emission from the high-Z plasmas. The recorded spectra were not temporally resolved and were spatially integrated over the varying plasma conditions along the line of sight of the HENWAY, which complicates the spectroscopic analysis and determination of plasma parameters.

We mention that L shell spectra from gold, lead, and uranium were first recorded by J.F. Seely *et al.* [24,25] using the High-Energy Electronic X-Ray Spectrometer (HENEX). The lead and uranium spectra were recorded from foils used a backlighters during experiments at the OMEGA laser facility. The gold spectra were recorded from a halfraums. The spectral range extended up to 15 keV and included the $4d \rightarrow 2p$ and $4p \rightarrow 2s$ type transitions. These Au transitions were better resolved than the $n=3 \rightarrow 2$ transitions presented here.

To interpret the recorded spectra and characterize these hot, high-Z plasmas, the radiation-hydrodynamics code LASNEX [26] was used to model the experiment. The LASNEX simulations predicted the electron temperatures and densities on a spatial and temporal grid along the line of sight of the spectrometer [1]. Emission spectra for each isosequence from Ne-like to Ni-like Au were generated by the hybrid-structure collisional-radiative code SCRAM [16], which uses atomic structure and transition rate data from the Flexible Atomic Code (FAC) [27,28]. The FLYCHK code [29] was used to calculate the CSD. We began by constructing line-integrated spectra at multiple times by folding the SCRAM, FLYCHK and LASNEX modeling along the HENWAY line of sight. Summing these spectra produced a simulated HENWAY spectrum that did not agree with the measured data. Obtaining good agreement with the measurements required reducing the electron temperatures predicted by LASNEX by a factor of 0.6.

2 Experiment

We present the analysis of a small hohlraum which was 600 μm in diameter, 660 μm in length, with a single laser entrance hole (LEH) and a back wall. The side walls were 40 μm thick and the back wall was 1 μm thick. The hohlraum was heated with nineteen beams from the OMEGA laser [13]. The spectral data reported here is from shot 41727. A schematic of the experimental geometry showing the target, the laser beams and the view of the relevant diagnostics is given in Fig. 1.

Three separate beam cones 1, 2 and 3 at 3ω light (351 nm) were fired into

the LEH. The pulse shape was square in time with a 1 ns duration as shown in Fig. 2. Cone 1 had 5 beams angled at 21.4° from the hohlraum axis. These beams were pointed and focused $450\text{ }\mu\text{m}$ in front of the LEH. Cone 2 had 5 beams at 42.0° . Cone 3 had 9 beams at 58.9° . Cones 2 and 3 were pointed and focused to the center of the LEH. All beams had distributed polarization rotators (DPRs) for beam smoothing [30]. The total energy delivered to the target was 8.84 kJ. Further details of this type of experiment are given in Refs. [1,2].

The DANTE is an absolutely calibrated low-resolution, soft x-ray spectrometer [31]. It measures the soft x-radiation emitted from the target. In the present geometry, DANTE viewed the target at 37.4° to the hohlraum axis. The target geometry combined with the integral of the flux from 0 to 2 keV is used to calculate the radiation temperature, T_{rad} . Shields (Pb-doped plastic or plastic-coated Ta) were used to confine the DANTE view to the region of interest. For shot 41727, the DANTE viewed the back wall of the target. A similar target, rotated 180° to give DANTE a view of the LEH, indicated the radiation temperature inside the hohlraum was $T_{rad} = 292\text{ eV}$. This was in agreement with LASNEX calculations [2].

The location of the plasma that emits x-rays in the L band region of gold (8 to 13 keV) can be determined by imaging a thin-walled hohlraum [1]. This shot used the same geometry as in Fig. 1 but the side walls of the target were $3.5\text{ }\mu\text{m}$ thick, so that they were transparent to L-band x-rays. X-ray images of the target were recorded as a function of time with a filtered x-ray pinhole snout attached to an x-ray framing camera [32]. The snout had a 8x magnification and recorded several images at different times during the experiment. The camera used $50\text{ }\mu\text{m}$ pinholes and $508\text{ }\mu\text{m}$ thick Al and $128\text{ }\mu\text{m}$ thick Be foils. This filter set significantly rejected x-rays with photon energies below $\approx 7\text{ keV}$. The filter transmissions at 10 keV and 5 keV were 0.05 and $< 10^{-9}$, respectively. Recorded images at $\approx 300, 600$ and 900 ps during the experiment are shown in Fig. 3. The thick Au walls of the reduced-scale hohlraum were opaque to 3 to 5 keV photons. The majority of the 3 to 5 keV and 8 to 13 keV x-rays recorded by the HENWAY were emitted from the laser entrance hole [1].

3 HENWAY Spectrometer

The Au spectra were recorded by the HENWAY crystal x-ray spectrometer [23]. The HENWAY has four channels in a convex crystal geometry to disperse the x-rays. DEF film was used as a recording media. Each channel typically has a different crystal to record a different spectral range onto photometrically calibrated DEF x-ray photographic film. Two channels were used

to record the L-band emission between 8 to 13 keV and the M-band emission between 3 to 5 keV. The HENWAY viewed the target with an angle of 63.4° to the cylindrical axis of the target. The HENWAY had no slit and is spatially integrating. The recorded spectrum is time integrated since no temporal gating system is available for the HENWAY spectrometer. For the 8 to 13 keV spectral region, the crystal was PET(002) with a 2d of 8.742 Å and had a 25.4 cm radius of curvature. For the 3 to 5 keV spectral region, the crystal was again PET(002) with a 2d of 8.742 Å and had a 21.6 cm radius of curvature. Each crystal mount was cut differently to select the correct angle to satisfy the Bragg equation for a given photon energy. The HENWAY was located ~ 185 cm from target chamber center. The DEF film was scanned into a digital image by a densitometer for analysis.

The energy dispersion of each HENWAY channel was determined by the energies of K absorption edges of several materials used as filters. The design of the HENWAY spectrometer allowed a complex set of different filters to be positioned before the crystal in the direction perpendicular to the plane of dispersion. Each filter set produced a different strip on the film image. For these experiments, four different sets of filters were used for both the 8 to 13 keV and the 3 to 5 keV channels and are given in Table 1. Three of the filter sets contained the K edge filters of Ge, Cu and V (L-Band) or Ti, Sc and V (M-Band) that were used to determine the dispersion curve. The dispersion was not linear in film position so three edge filters were necessary. The fourth strip was used to determine the intensity of the emission and did not contain any edge filters. A typical spectral image from the 8 to 13 keV channel is shown in the top of Fig. 4. The lineouts for each strip in film density versus position in cm are shown in frames A to D. A similar image was recorded for the 3 to 5 keV channel. The position on the film, x , in cm of each edge was determined from the lineouts. A 2^{nd} order polynomial was fit to the data of absorption edge energy versus position to determine the dispersion. The fit for the 8 to 13 keV channel was

$$E(keV) = 4.8424 + 0.28598x + 0.060889x^2$$

which gave a correlation coefficient $R = 1$. The fit is shown in Fig. 5 with the three calibration points. A similar dispersion curve was generated for the 3 to 5 keV spectrum.

The measured film density from the lineouts was converted to absolutely calibrated flux units of $keV/4\pi\text{-keV}$. Details of the geometry and the analytical equations describing the HENWAY instrument are given by Koppel *et al.* [23]. The sensitivity of the spectrometer can be expressed as:

$$S(E) = T(E)D(E)\frac{\Omega}{4\pi}\frac{R(\theta)}{E}\left(\frac{\Delta x}{\Delta\theta}\right)/\left(\frac{\Delta x}{\Delta E}\right)$$

The variables, $T(E)$, Ω and $R(\theta)$ are the transmissions of the filters, solid angle subtended by the spectrometer and the integrated reflectivity of the crystal, respectively. The crystal reflectivities chosen were the average of the mosaic model and the Darwin-Prins relation given by Henke *et al.* [33]. Measurements by Gilfrich *et al.* [34] indicated that the PET reflectivities have the same response as a function of energy as the average Henke values. However, the absolute reflectivities are roughly half of the values we have used. This is an indication of the error bars on the absolute line emission values presented here. The filter transmissions were taken from the Center for x-ray Optics (CXRO) at University California Berkeley [33,35,36].

An optical densitometer was used to determine the optical density of the developed film. The optical density must be converted to units of photons/cm² for comparison with the simulations. The conversion factor, $D(E)$, has been well document by Henke *et al.* [37–39]. This method is used to calibrate the film. The factor $\frac{\Delta x}{\Delta\theta} / \frac{\Delta x}{\Delta E}$ is the variation of photon energy as a function of angle along the position on the film. This is just the dispersion of the spectrometer. A sample spectrum is given in Fig. 6 and Fig. 7 in flux units of keV/4 π -keV. The intensities were converted to ph/4 π -eV for comparison with the spectral modeling.

The spectral resolution for the 3 to 5 keV channel determined from the recorded spectral images was ~ 5 eV which was adequate to resolve individual spectral lines. For the 8 to 13 keV channel, the spectral features were too blended to determine the spectral resolution. Several factors contribute to the resolution of both recorded spectra, including the crystal resolution, the film grain size, and the effect of the finite source size. The crystal resolving power is large and about 6000 [40]. The grain size of the film is 1.6 μm in diameter and is not resolution limiting [37–39]. The spectral resolution of the HENWAY was limited by the size of the target for both spectral ranges. This effect could be determined from geometric considerations and the analytical solutions given by Koppel *et al.*. This formalism correctly predicted the dispersion curve of the HENWAY and was used to predict the spectral resolution, which is given as a function of photon energy in Fig. 5 for a 600 μm target. The resolution was ~ 30 eV at a photon energy of 10 keV.

4 Atomic Physics and Spectral Modeling

4.1 LASNEX Modelling

The radiation-hydrodynamics code LASNEX [26] was used to simulate the conditions of the plasma created inside the laser heated target under the experimental conditions. Details of the modeling are given in Ref. [2] for a reduced-scale hohlraum which is 600 μm in diameter and 600 μm in length. The incident laser energy was 9.5 kJ, spread among three cone angles in a 1 ns square laser pulse. The total energy used in the simulations was $\sim 7\%$ larger than the measured total energy. Fig. 8 and Fig. 9 show the temperatures and densities of the plasma along the line of sight of the HENWAY spectrometer as a function of time. The simulations predicted a T_{rad} of ~ 300 eV as seen by the DANTE. Since most of the 3 to 5 keV and 8 to 13 keV emission recorded by the HENWAY is assumed to be emitted from the hot LEH region (Fig. 3), the synthetic spectra were calculated along a line of sight of the HENWAY which was 63.4° to the LEH axis. Temperatures and densities for this line of sight on a grid with 10 μm spacing outside the LEH and 5 μm spacing inside were tabulated every 100 ps from 400 to 1300 ps. These profiles were combined with CSD and line emission modeling to create simulated spectra for comparison with the recorded HENWAY spectra.

4.2 CSD Modeling

FLYCHK is a simple and fast tool to provide ionization and population distributions of laboratory plasmas in zero dimensions with reasonable accuracy. Its application is general enough to study low to high Z ions for steady-state or time-dependent cases. FLYCHK is useful for CSD calculations and time dependent modeling but uses less accurate atomic structure than an atomic structure code like the Flexible Atomic Code (FAC) [27,28]. FLYCHK has been compared with codes with detailed atomic structures in a series of Non-LTE kinetics code comparison workshops [20,21] and found to give results comparable to those of detailed codes within 1-2 charge states for plasma conditions often found in laboratory plasmas. Since collisional-radiative calculations based on complete detailed atomic structure can be computationally expensive, FLYCHK was used to calculate the CSD for the gold plasma created in this experiment.

FLYCHK solves rate equations by using collisional and radiative processes. The energy levels are based on the hydrogenic expressions [41] with a few key lookup tables. Each hydrogenic level for each ionization stage is described by

the principal quantum number of ‘n’. The ionization potential of an excited level with an outermost bound electron of principal quantum number ‘n’ is computed using the hydrogenic approximation with relativistic corrections. For accuracy and consistency with the existing FLY, empirical ionization energies for the ground states are used [42]. Autoionizing inner-shell excited levels are included in the hydrogenic approximation.

The collisional and radiative processes are not computed *ab initio* as they are in FAC. The rates are based on previously published analytic formalisms. These formalisms allow much faster computations sacrificing some accuracy. The collisional excitation cross-sections are based on oscillator strength for the allowed transitions [43]. The same formalism is used for inner-shell excitation processes.

For better accuracy, an option to use fitted coefficients based on elements is also implemented in the code. [44] A semi-empirical formula of Burgess and Chidichimo [45] is used for collisional ionization from a level ‘n’.

An absorption oscillator strength of a transition from a level ‘n’ to a level ‘m’ uses hydrogenic oscillator strengths. The oscillator strength together with Einstein’s relation are used to generate the spontaneous and stimulated emission rates and absorption coefficients for radiative bound-bound transitions. For bound-free processes, Kramers’ quasi-classical photoionization cross-sections are used [46]. Using detailed balance and photoionization rate coefficients, the spontaneous radiative recombination rate coefficients are generated.

The two processes involving inner-shell excited level autoionization and inner-shell photoionization are implemented with atomic data generated by jj configuration average codes. K- and L-shell photoionization cross-sections are computed for hydrogenic levels by using Hartree-Fock-Slater wave functions [47,48]. Autoionization rates are calculated by perturbation theory in the Dirac-Hartree-Slater approach [49,50].

Dielectronic recombination processes are included via electron capture processes, whose rates are determined by detailed balance. It should be noted, however, that due to the hydrogenic approximation, $n = 0$ transitions are not included and these contributions can be the dominant dielectronic recombination processes at low temperatures.

FLYCHK was used to calculate the CSD on a grid of temperatures from 1 keV to 50 keV. The grid between 3 and 10 keV was spaced every 1 keV. The grid was every 5 keV for temperatures greater than 10 keV. The calculated CSDs are plotted in Fig. 10 for $n_e = 10^{21} \text{ cm}^{-3}$. The average $\langle q \rangle$ predicted by FLYCHK as a function of temperature are shown in Fig. 11 at electron densities of 10^{20} , 10^{21} and 10^{22} cm^{-3} . The $\langle q \rangle$ is very similar for densities less than 10^{21} , but increased by about 5% at $\sim 10^{22}$. The CSD for each LASNEX

temperature was determined through a linear interpolation of the calculated FLYCHK CSDs. The FLYCHK CSD at the temperature just above and below each LASNEX temperature were used as the interpolation basis. The total fraction of each interpolated CSD was normalized to one. This procedure created a grid of CSDs as a function of space and time along the line of sight of the HENWAY spectrometer.

4.3 *Line Emission Modeling*

The hybrid-structure collisional-radiative model SCRAM [16] was used to generate synthetic M- and L-shell spectra for Ne-like to Ni-like Au ions. SCRAM uses atomic structure and transition rates calculated using the FAC atomic data package [27,28]. FAC calculates energy level structures from the Dirac equation with a parametric potential and provides radiative transition and autoionization rates along with collisional excitation, collisional ionization, and photoionization cross sections which are integrated over the electron and photon distribution functions to obtain direct rates coupling the energy levels. Reverse rates of three-body recombination, radiative recombination, and dielectronic capture are calculated using detailed balance.

Generally, fine-structure energy levels with full treatment of configuration interaction effects are necessary to obtain spectroscopic-quality model predictions. Models based on relativistic configuration averaged levels that exclude configuration interaction effects and enforce strict jj coupling do not have the accuracy necessary to fit experimental data: they may give energies for L-shell transitions in Au ions that are shifted by as much as 50 eV from fine structure calculations and experimental values. However, a complete fine structure model with open M- and L-shells might have more than $\sim 10^8$ levels in a single M-shell ion and would be computationally intractable.

Based on the procedures described in [16], we have developed a computationally tractable hybrid model which combines fine structure data for a limited subset of coronal levels (levels accessible via a single excitation from the ground configuration) with a complete set of relativistic configuration-averaged levels. Ions from Ne to Ni-like Au are included, each with at least all of the configurations belonging to the superconfiguration (SCs) that are listed in Table 2. Effects due to configuration interaction and departures from jj coupling on line positions and strengths in each ion are propagated from transitions among fine structure levels to all transitions among the relativistic configuration-averaged levels with the same underlying initial and final nlj . We note that the hydrogenic structure used by FLYCHK is much more extensive than the SC structure used in the hybrid model, with singly excited electrons from the valence and inner-shells and doubly excited electrons from

the valence shell up to $n=10$. Although such states do not contribute much to the emission, they are critical for accurate predictions of the charge state distribution, particularly through the inclusion of dielectronic recombination channels in the doubly excited SCs. The $\langle q \rangle$ calculated by SCRAM with the restricted set of SCs listed in Table 2 tend to be higher than the FLYCHK $\langle q \rangle$ by about three charge states.

The restricted-structure, partially averaged hybrid model has $\sim 10^6$ levels, which exceeds the memory constraints on many computers. Therefore, the hybrid structure is further averaged within the SCRAM code before the collisional-radiative rate matrix is solved. In this second averaging, fine-structure and relativistic configurations are retained in the ground superconfigurations but all other levels are averaged into non-relativistic configurations. This cuts down the number of levels in the solver to $\sim 10^4$. All of the rates are computed individually and averaged to obtain a $10^4 \times 10^4$ rate matrix that is solved for the averaged level populations. Before constructing synthetic spectra, SCRAM uses these averaged-level populations and stored rates between SCs and the levels of the original hybrid model to obtain better-than-statistical populations for the original set of hybrid-structure levels. Each level in each non-ground-SC is populated according to the populations of the ground SCs in its own ion and its neighbors multiplied by their total rates into the original hybrid-model level, roughly following the procedure given in [51]. This procedure recaptures the non-statistical character of levels that were averaged prior to solving the rate matrix. To prevent bias from an inconsistent CSD in the individual-ion emission spectra, we have imposed a uniform CSD on the SCRAM calculations – a reasonable approximation for the dominant ions in broad mid-shell CSDs.

The original radiative decay rates and transition energies are used with the final hybrid level populations to construct synthetic spectra. Line emission spectra from each iso-sequence from Ni- to Ne-like Au were generated for photon energies from 2 to 15 keV for $n_e = 3 \times 10^{21}$ for T_e from 4 to 10 keV every 1 keV. These emission spectra were then combined with the LASNEX and FLYCHK modeling to compare with the recorded HENWAY data. At each temperature and density point on the grid described above, the line emission $I_{SCRAM}(\text{iso}, T(x, t))$ (in ph/ion/s) from each iso-sequence was multiplied by the relative ionic fraction predicted by FLYCHK, $F_{FLYCHK}(\text{iso}, T(x, t))$ and then convolved with the spectral response function of the HENWAY. (The line emission was not interpolated between each LASNEX temperature on the grid but rather the spectrum calculated at the temperature nearest to the LASNEX temperature was used.) The spectrum at a given time is thus (see Fig. 12):

$$I(t) = \sum_x * C * I_{SCRAM}(\text{iso}, T(x, t)) [ph/sec/ion] *$$

$$F_{FLYCHK}(iso, T(x, t)) * n_{Ion}[particles * cm^{-3}] * V(x)[cm^3]$$

where n_{Ion} is proportional to the electron density assuming a neutral plasma, V is the volume of each grid, C is a constant, and the sum is done over the line of sight, x . The final time-integrated spectrum is then the sum of $I(t)$ over time.

Opacity effects due to re-absorption of the emitted lines are not included in the modeling presented here. Although, reabsorption can reduce the intensities of the L-shell lines by fractions of 0.5 to 0.8 over a few hundred μm of uniform plasma, opacity effects will not influence the first-order diagnostic characteristic of the calculated spectra, which is the central emission energy of the L-shell features.

5 Spectral Line Analysis

The calibrated spectrum recorded by the HENWAY between 8 to 13 keV is shown in Fig. 6. It comprises three broad features of L-Band gold whose individual lines are not resolved by the spectrometer. The three features were identified through comparisons with the SCRAM/FAC modeling to be emission from Co to Ne-like Au. The feature at 9 keV was the least intense and contains the $2p^2_{1/2}2p^3_{3/2}3s^23p^k3d^{k'} \rightarrow 2p^63s3p^k3d^{k'}$ transitions. The feature at 10 keV was the most intense and contains the transitions of the type $2p^2_{1/2}2p^3_{3/2}3s^k3p^{k'}3d^{k''}3d_{5/2} \rightarrow 2p^63s^k3p^{k'}3d^{k''}$. The feature at 12 keV contains the $2p_{1/2}2p^4_{3/2}3s^k3p^{k'}3d^{k''}3d_{3/2} \rightarrow 2p^63s^k3p^{k'}3d^{k''}$ transitions.

The calibrated M-shell spectrum recorded between 3 to 5 keV is shown in Fig. 7. The identified transitions are $5f_{5/2} \rightarrow 3d_{3/2}$ from Fe-like to P-like gold [52]. Other M-shell transitions such as $5f_{7/2} \rightarrow 3d_{5/2}$, $4p_{3/2} \rightarrow 3s_{1/2}$, and $4d_{3/2} \rightarrow 3p_{1/2}$ on the low-energy side of the $5f_{5/2} \rightarrow 3d_{3/2}$ transitions also contribute to the emission.

The simulated L- and M-shell spectra are compared with the recorded spectra in Figs. 13 and Fig. 14, respectively. The spectra calculated using the electron temperature predictions from LASNEX appear to be over-ionized and are in rather poor agreement with the measured data. The central charge state inferred from the measured spectra is near Ti-like Au (Au^{57+}) which is about 6 charge states lower than the P- or S-like ($Au^{63+-64+}$) central charge state predicted by FLYCHK at the LASNEX electron temperatures. Introducing a scaling factor of 0.6 to globally adjust the LASNEX temperatures downwards brought the simulated spectra into good agreement with the experimental data, as shown in Fig. 13 and Fig. 14. The CSD from FLYCHK varies slightly with electron density (see Fig. 11) and introduces some uncertainty into the

comparison. The scaling factor was determined using the FLYCHK CSD at 10^{20} cm^{-3} and 10^{22} cm^{-3} to be 0.6 and 0.55, respectively. The variation was on the order of 5%.

As mentioned above, opacity effects have not been included in the modeling. Including opacity effects might slightly improve the agreement with experiment by bringing up the relative intensity of the early-time, low-density and low-energy features, since opacity effects are approximately equal for all dominant charge states at a given density and become less significant with decreasing density. Reabsorption is a second-order effect on the present analysis, since it has no effect on the position of the emission features and its effect on line intensities is less dramatic than the quadratic dependence of intensity on the electron density. Therefore, including this effect should not effect the central emission energy of the features.

Previous comparisons of LASNEX modeling to measured radiation flux and radiation temperature (Fig. 2) have shown excellent agreement [1–3] for experiments using the multiple beam cone geometry in Fig. 2. LASNEX has sometimes underpredicted plasma filling and radiation temperature for a simpler geometry where a single laser beam is incident along the hohlraum axis [53].

The experimental line-averaged and time-integrated CSD from the HENWAY spectral analysis can be compared with FLYCHK CSD predictions to give an estimate for the average temperature of the plasma. The CSD predictions from FLYCHK for electron temperatures of 6, 6.5, 7 and 8 keV are given in Fig. 15 for $n_e = 10^{21} \text{ cm}^{-3}$. The CSD at 6.5 keV is interpolated. The line-averaged CSD from the LASNEX/HENWAY comparison using a scaling factor of 0.60 is plotted as black squares. The experimentally inferred CSD is between FLYCHK prediction of 6.0 and 6.5 keV.

The electron temperature helps describes plasma conditions in the highly non-LTE laser deposition region. Recent comparisons of non-LTE codes for gold plasmas in the temperature and density range of interest show variations in predicted T_e of 1.8 keV for $\langle q \rangle \sim 53$ at $n_e = 10^{21} \text{ cm}^{-3}$ [54]. The data and analysis described in this paper can be used to benchmark the codes. However, the electron temperature has never been directly measured on these experiments.

6 Conclusions

M-Band and L-Band gold spectra have been recorded between 3 to 5 keV and 8 to 13 keV from a reduced-scale gold hohlraum target heated with $\sim 9 \text{ kJ}$ from the OMEGA laser. The line emission has been identified as $3d_{3/2} \rightarrow 2p_{1/2}$, $3d_{5/2} \rightarrow 2p_{3/2}$, and $3s \rightarrow 2p$ transitions from Ne-like to Co-like Au in the L-Band

and $5f \rightarrow 3d$, $4d \rightarrow 3p$, and $4p \rightarrow 3s$ transitions from Fe-like to P-like Au in the M-Band. The radiation-hydrodynamics code LASNEX, collisional-radiative codes FLYCHK and SCRAM, and the atomic structure code FAC were used to simulate the conditions in the reduced scale hohlraum targets and to construct synthetic spectra for comparison with the measured time- and space-integrated emission. Initial comparisons between the modeling and the experiment suggested that the electron temperatures predicted by LASNEX were too high by a significant factor. Agreement was obtained by scaling the predicted T_e from LASNEX by 0.6, and the average temperature of the plasma was determined to be between 6.0 and 6.5 keV.

7 Acknowledgments

We thank the excellent OMEGA laser crew at the Laboratory for Laser Energetics for their expert help in these experiments. We thank Dr. Klaus Widmann for very useful discussions. This work was performed under the auspices of the U.S. Department of Energy by Lawrence Livermore National Laboratory in part under Contract W-7405-Eng-48 and in part under Contract DE-AC52-07NA27344 and under grant number DE-FG52-2005NA26017 (National Laser Users Facility).

References

- [1] M. B. Schneider, D. E. Hinkel, O. L. Landen, D. H. Froula, R. F. Heeter, A. B. Langdon, M. J. May, J. McDonald, J. S. Ross, M. S. Singh, L. J. Suter, K. Widmann, B. K. Young, H. A. Baldis, C. Constantin, R. Bahr, V. Yu. Glebov, W. Seka, and C. Stoeckl, *Physics of Plasmas* **13**, 112701 (2006).
- [2] M. B. Schneider, D. E. Hinkel, S. J. Moon, S. B. Hansen, H. A. Baldis, C. Austheim-Smith, G. V. Brown, K. M. Campbell, H. K. Chung, K. Cone, C. G. Constantin, V. Yu. Glebov, J. P. Holder, G. Holland, D. L. James, A. B. Langdon, R. W. Lee, M. J. May, S. Roberts, J. Schein, J. Seely, W. Seka, R. Shepherd, M. S. Singh, C. Stoeckl, R. E. Turner, F. Weber, K. Widmann, and B. K. Young, *High Energy Density Physics* **3**, 256-262 (2007).
- [3] D. E. Hinkel, M. B. Schneider, H. A. Baldis, R. E. Bonanno, D. E. Bower, K. M. Campbell, J. R. Celeste, S. Compton, R. Costa, E. L. Dewald, S. N. Dixit, M. J. Eckart, D. C. Eder, M. J. Edwards, A. Ellis, J. A. Emig, D. H. Froula, S. H. Glenzer, D. Hargrove, C. A. Haynam, R. F. Heeter, M. A. Henesian, J. P. Holder, G. Holtmeier, L. James, K. S. Jancaitis, D. H. Kalantar, J. H. Kamperschroer, R. L. Kauffman, J. Kimbrough, R. K. Kirkwood, A. E. Koniges, O. L. Landen, M. Landon, A. B. Langdon, F. D. Lee, B. J. MacGowan, A. J. Mackinnon, K.

- R. Manes, C. Marshall, M. J. May, J. W. McDonald, J. Menapace, E. A. Moses, D. H. Munro, J. R. Murray, C. Niemann, D. Pellinen, V. Rekow, J. A. Ruppe, J. Schein, R. Shepherd, M. S. Singh, P. T. Springer, C. H. Still, L. J. Suter, G. L. Tietbohl, R. E. Turner, B. M. Van Wonterghem, R. J. Wallace, A. Warrick, P. Watts, F. Weber, P. J. Wegner, E. A. Williams, B. K. Young, P. E. Young, *Physics of Plasmas* **12**, 056305 (2005).
- [4] B.J. MacGowan, B.B. Afeyan, C.A. Back, R.L. Berger, G. Bonnaud, M. Casanova, B.I. Cohen, D.E. Desenne, D.F. DuBois, A.G. Dulieu, K.G. Estabrook, J.C. Fernandez, S.H. Glenzer, D.E. Hinkel, T.B. Kaiser, D.H. Kalantar, R.L. Kauffman, R.K. Kirkwood, W.L. Kruer, A.B. Langdon, B.F. Lasinski, D.S. Montgomery, J.D. Moody, D.H. Munro, L.V. Powers, H.A. Rose, C. Rousseaux, R.E. Turner, B.H. Wilde, S.C. Wilks, and E.A. Williams, *Phys. Plasmas* **3**, No.5, 2029 (1996).
- [5] D. E. Hinkel, M. B. Schneider, E. A. Williams, A. B. Langdon, L. J. Suter, and P. T. Springer, Third International Conference on Inertial Fusion Sciences and Applications, 2003, edited by B.A. Hammel, D.D. Meyerhofer, J. Meyer-ter-Vehn, H. Azechi (American Nuclear Society, Inc.,) 242-246 (2004).
- [6] A. B. Langdon and D. E. Hinkel, *Phys. Rev. Lett.* **89**, 015003 (2002).
- [7] C. Stoeckl, R.E. Bahr, B. Yaakobi, W. Seka, S.P. Regan, R.S. Craxton, J.A. Delettretz, R.W. Short, J. Myatt, A.V. Maximov and H. Baldis, *Phys. Rev. Lett.* **90**, 235002 (2003).
- [8] E. M. Campbell, *Laser Part. Beams* **9**, 209 (1991)
- [9] M. E. Foord, S. H. Glenzer, R. S. Thoe, K. L. Wong, K. B. Fournier, B. G. Wilson and P. T. Springer, *Phys. Rev. Lett.* **85**, 992 (2000).
- [10] A. Bar-Shalom, M. Klapisch and J. Oreg, *Jour. of Quant. Spect. and Rad. Trans.* **71**, 169 (2001).
- [11] S. H. Glenzer, K. B. Fournier, B. G. Wilson, R. W. Lee and L. J. Suter, *Phys. Rev. Lett.* **87**, 045002 (2001).
- [12] B. G. Wilson *et al*, in *Radiative Properties of Hot Dense Matter*, edited by W. Goldstein, C. Hooper, J. Gauthier, J. Seely, and R. Lee, World Scientific, Singapore, (1991).
- [13] T. R. Boehly, R. S. Craxton, T. H. Hinterman, J. H. Kelly, T. J. Kessler, S. A. Kumpan, S. A. Letzring, R. L. McCrory, S. F. B. Morse, W. Seka, S. Skupsky, J. M. Soures, and C. P. Verdon, *Rev. Sci. Instrum.* **66**, 508 (1995).
- [14] R. F. Heeter, S. B. Hansen, P. Beiersdorfer, M. E. Foord, K. B. Fournier, D.H. Froula, A. J. Mackinnon, M. J. May, M. B. Schneider, and B.K.F. Young, *Proceedings of Atomic Processes in Plasmas 2004* edited by J.S. Cohen, S. Mazevet, and D.P. Kilcrease, p. 103. (2004).
- [15] R. F. Heeter, S. B. Hansen, K. B. Fournier, M. E. Foord, D. H. Froula, A. J. Mackinnon, M. J. May, M. B. Schneider, and B.K.F. Young, *Phys. Rev. Lett.* **99** 195001 (2007).

- [16] S.B. Hansen, J. Bauche, C. Bauche-Arnoult, and M.F. Gu, High Energy Density Physics **3**, 109-114 (2007).
- [17] C. Chenais-Popovics, V. Malka, and J.-C. Gauthier, S. Gary, O. Peyrusse, and M. Rabec-Le Gloahec, I. Matsushima, C. Bauche-Arnoult, A. Bachelier, and J. Bauche, Phys. Rev. E., **65** 046418, (2002).
- [18] R.W. Lee, J.K. Nash, and Y. Ralchenko, J. Quant. Spectrosc., Radiat. Transfer **58**, 737 (1997).
- [19] C. Bowen, A. Decoster, C.J. Fontes, K.B. Fournier, O. Peyrusse, and Yu. V. Ralchenko, J. Quant. Spectrosc. Radiat. Transfer **81**, 71 (2003).
- [20] C. Bowen, R.W. Lee and Yu. Ralchenko, J. Quant. Spectrosc., Radiat. Transfer **99**, 102-119 (2006).
- [21] J.G. Rubiano, R. Florido, C. Bowen, R.W. Lee and Yu. Ralchenko, High Energy Density Physics, **3**, 225-232 (2007).
- [22] K.L. Wong, M.J. May, P. Beiersdorfer, K.B. Fournier, B. Wilson, G.V. Brown, and P. Springer P.A. Neill and C.L. Harris, Phys. Rev. Lett. **90** 235001 (2003).
- [23] L. N. Koppel and J. D. Eckels, UCRL-79781 (October 1977).
- [24] J.F. Seely, R. Doron, A. Bar-Shalom, L.T. Hudson, C. Stoeckl Journal of Quantitative Spectroscopy and Radiative Transfer, **81** 421 (2003).
- [25] J.F. Seely, C.A. Back, C. Constantin, R.W. Lee, H.-K. Chung, L.T. Hudson, C.I. Szabo, A. Henins, G.E. Holland, R. Atkin, L. Marlin, Journal of Quantitative Spectroscopy and Radiative Transfer, **99** 572 (2006).
- [26] G. Zimmerman and W. L. Kruer, Comments Plasma Phys. Controlled Fusion **2**, 51 (1975).
- [27] M. F. Gu, et al., ApJ **582**, 1241 (2003).
- [28] M. F. gu, Can. J. Phys. **86**, 675 (2008).
- [29] H.-K. Chung, M. Chen, W. L. Morgan Y. Ralchenko, and R. W. Lee, High Energy Density Physics, **1**, p.3 (2003).
- [30] T. R. Boehly, V. A. Smalyuk, D. D. Meyerhofer, J. P. Knauer, D. K. Bradley, R. S. Craxton, M. J. Guardalben, S. Skupsky, and T. J. Kessler, J. Appl Physics **85**, 3444 (1999).
- [31] H. N. Kornblum, R. L. Kauffman, and J. A. Smith, Rev. Sci. Instrum. **57**, 2179 (1986).
- [32] K. S. Budil, T. S. Perry, P. M. Bell, *et al.*, Rev. Sci. Instrum. **67**, (1996) 485.
- [33] B. L. Henke, E. M. Gullikson and J. C. Davis, Atomic Data and Nuclear Data Tables **54**, 181 (1993).

- [34] J. V. Gilfrich, D. B. Brown and P. G. Burkhalter, Appl. Spectrosc. **29**, 322 (1975).
- [35] R. Soufli, S. Bajt and E. M. Gullikson, SPIE Proceedings **3767**, 251-8 (1999).
- [36] E. M. Gullikson, P. Denham, S. Mrowka, J. H. Underwood, Physical Review B **49**, 16283-8 (15 June 1994).
- [37] B.L. Henke, S.L. Kwok, J.Y. Uejio, H.T. Yamada and G.C. Young, Journal of the Optical Society of America B **1**, 818 (1984).
- [38] B. L. Henke, F. G. Fujiwara M. A. Tester, C. H. Dittmore and M. A Palmer, Journal of the Optical Society of America B **1**, 828 (1984).
- [39] B. L. Henke, J. Y. Uejio, G. F. Stone, C. H. Dittmore and F.G Fujiwara, Journal of the Optical Society of America B **3**, 1540 (1986).
- [40] A. Burek, Space Science Instrumentation **2**, 53 (1976).
- [41] Y. T. Lee, JQSRT **38**, 131 (1987).
- [42] R. L. Kelly and L. J. Palumbo, Technical report no. NRL-7599, NRL Report, (1973).
- [43] H. Van Regemorter, Ap J **136**, 906 (1962).
- [44] H.-K. Chung, M.H. Chen and R.W. Lee, High Energy Density Physics, Vol 3, p.342-352 (2007)
- [45] A. Burgess, MC Chidichimo, Mon Not R Astron Soc **203**, 1269 (1983).
- [46] H. Kramers, Philos Mag **46**, 836 (1923).
- [47] J. H. Scofield, Phys Rev A **40**, 3054 (1989).
- [48] E. B. Saloman, J. H. Hubbell, J. H. Scofield, At Data Nucl Data Tables **38**, 1 (1988).
- [49] M. Chen, E. Laiman, B. Crasemann, M. Aoyagi, H. Mark, Phys Rev A **19**, 2253 (1979).
- [50] S. Perkins, D. Cullen, M. Chen, J. Hubbel, J. Rathkopf, JH Scofield, Technical report no. UCRL-50400 V.30, Lawrence Livermore National Laboratory, (1991).
- [51] F. B. Rosmej, Europhys. Lett. **76**, 1081 (2006).
- [52] M. J. May, P. Beiersdorfer, G. V. Brown, K. B. Fournier, M. Gu, S. B. Hansen, M. Schneider, J. H. Scofield, S. Terracol, K. J. Reed, B. Wilson, K. L. Wong, K. R. Boyce, R. Kelley, C. A. Kilbourne and F. S. Porter, Can. J. Phys. **86**, 251 (2008).
- [53] M. B. Schneider, D. E. Hinkel, B. K. Young, J. P. Holder, A.B. Langdon, H.A. Baldis, R. Bahr, D. E. Bower, H. C. Bruns, K. M. Campbell, J. R. Celeste, S. Compton, C. G. Constantin, R. L. Costa, E. L. Dewald, S. N. Dixit, M. J. Eckart, D. C. Eder, M. J. Edwards, A. D. Ellis, J. A. Emig, D. H. Froula, V. Glebov,

- S. H. Glenzer, D. Hargrove, C. A. Haynam, R. F. Heeter, M. A. Henesian, G. Holtmeier, D. L. James, K. S. Jancaitis, D. H. Kalantar, J. H. Kamperschroer, R. L. Kauffman, J. Kimbrough, R. Kirkwood, A. E. Koniges, O. L. Landen, M. Landon, F.D. Lee, B. J. MacGowan, A. J. Mackinnon, K. R. Manes, C. Marshall, M. J. May, J. W. McDonald, J. Menapace, S. J. Moon, E.I. Moses, D. H. Munro, J. R. Murray, C. Niemann, D. Pellinen, K. Piston, G. D. Power, V. Rekow1, S. Roberts, J. A. Ruppe, J. Schein, W. Seka, R. Shepherd, M. S. Singh, C. Sorce, P. T. Springer, C.H. Still, C. Stoeckl, L. J. Suter, G. L. Tietbohl, R. E. Turner, B. M. Van Wonterghem, R. J. Wallace, A. Warrick, P. Watts, F. Weber, P. J. Wegner1, E. A. Williams, P.E. Young, J. Phys. IV, **133**, 1205-1208, (2006).
- [54] G. V. Brown, S. B. Hansen, E. Trabert, P. Beiersdorfer, H. Chen, H. K. Chung, J. H. T. Clementson, M. F. Gu, D. B. Thorn, and K. Widmann, Phys. Rev. E 77, 066406 (2008).

Table 1

Filters used in the HENWAY

Channel	Line Out	Front Filter	Edge Filter	Edge Energy (keV)
8 - 13 keV	A	12 μm Al/25 μm Be	25 μm V	5.465
8 - 13 keV	B	12 μm Al/25 μm Be	-	-
8 - 13 keV	C	25 μm Be	25 μm Cu	8.979
8 - 13 keV	D	75 μm Be	10 μm Ge	11.103
3 - 5 keV	A	25 μm Be	10 μm V	5.465
3 - 5 keV	B	25 μm Be	-	-
3 - 5 keV	C	12 μm Al/25 μm Be	12.5 μm Sc	4.492
3 - 5 keV	D	12 μm Al/25 μm Be	12.5 μm Ti	4.966

Table 2

Superconfigurations included in the SCRAM/FAC modelling. Here, ‘n’ is the principle quantum number of a given shell and N is the number of electrons in that shell.

n = 1	n = 2	n = 3	n = 4
(1)2	(2)8	(3)N	
(1)2	(2)8	(3)N-1	(4)1
(1)2	(2)8	(3)N-1	(5)1
(1)2	(2)7	(3)N+1	
(1)2	(2)7	(3)N	(4)1

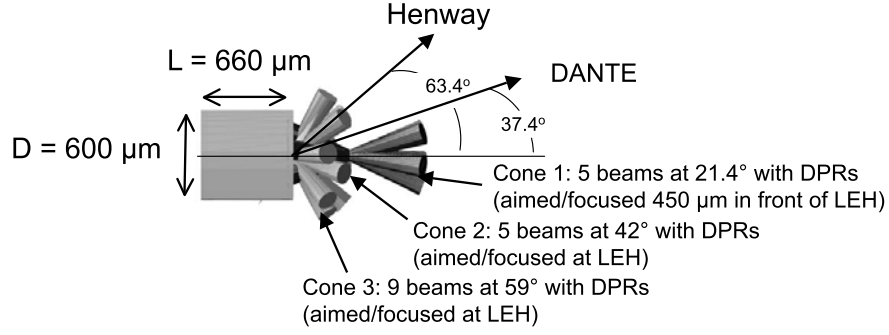


Fig. 1. Schematic of reduced-scale hohlraum targets shot at the OMEGA laser and the laser beams used. Note that beams in three cone angles heat the target.

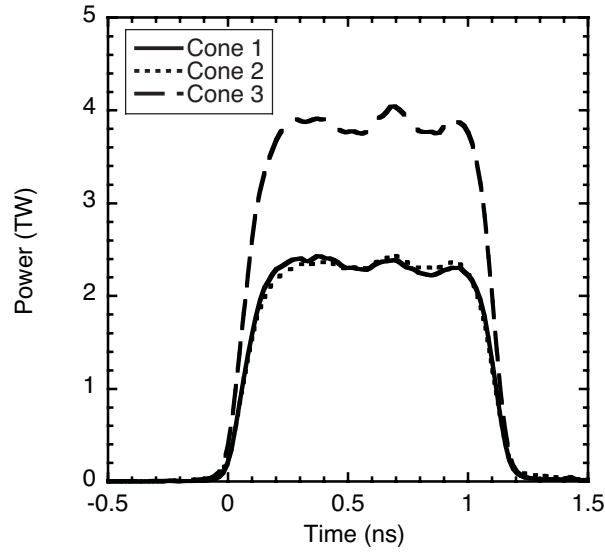


Fig. 2. Time evolution of the 1 ns beam pulse used to heat the target.

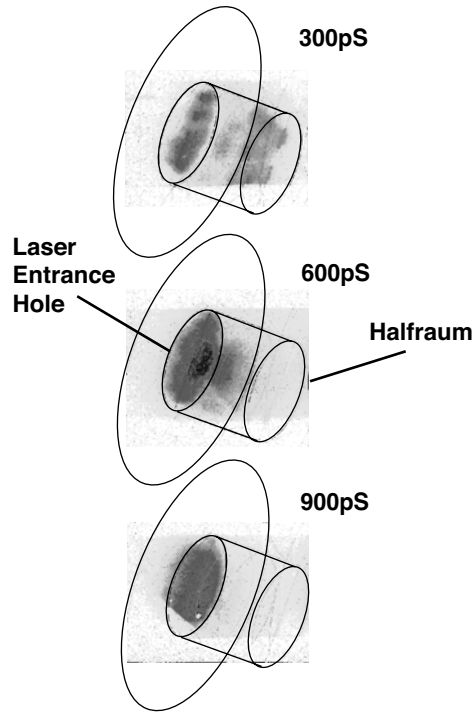


Fig. 3. Time resolved pinhole camera images of the target filtered for > 7 keV photons.

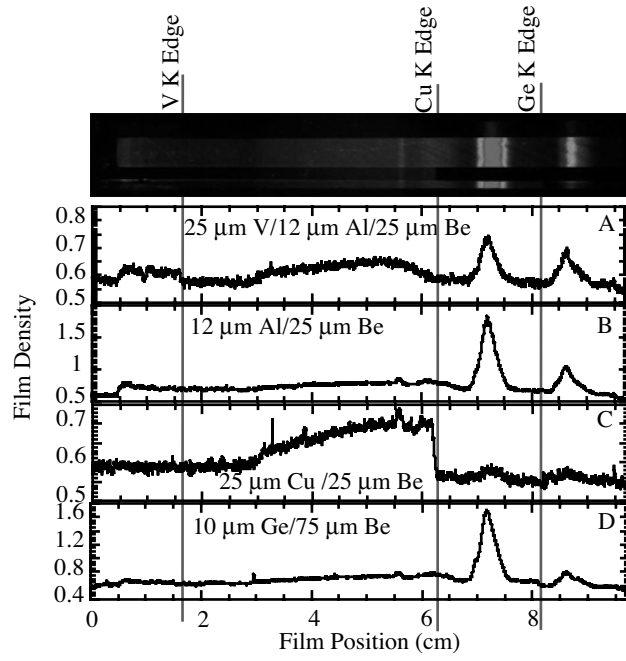


Fig. 4. Spectral photograph recorded by the HENWAY between 8 to 13 keV. Lineouts from all four filter combinations are shown below the film image with each filter edge marked.

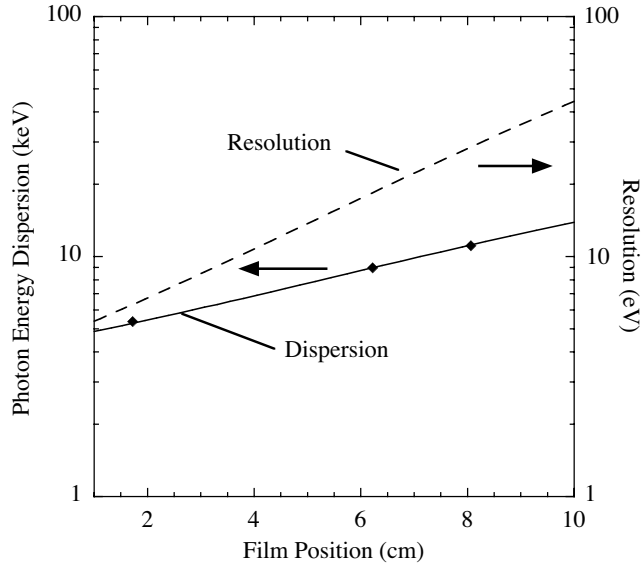


Fig. 5. Plot of photon energy calibration (keV) and spectral resolution (eV) for the 8 to 13 keV HENWAY channel as a function of position on the film in cm. Locations of the filter edges used as photon energy calibration references are represented by diamonds. The fit is the solid line.

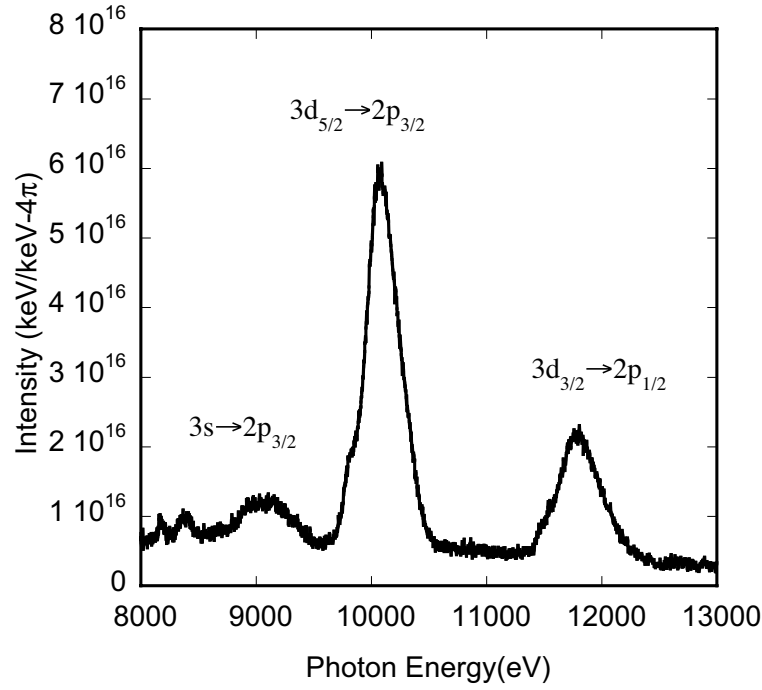


Fig. 6. Calibrated spectra from the HENWAY between 8 to 13 keV for OMEGA shot 41727.

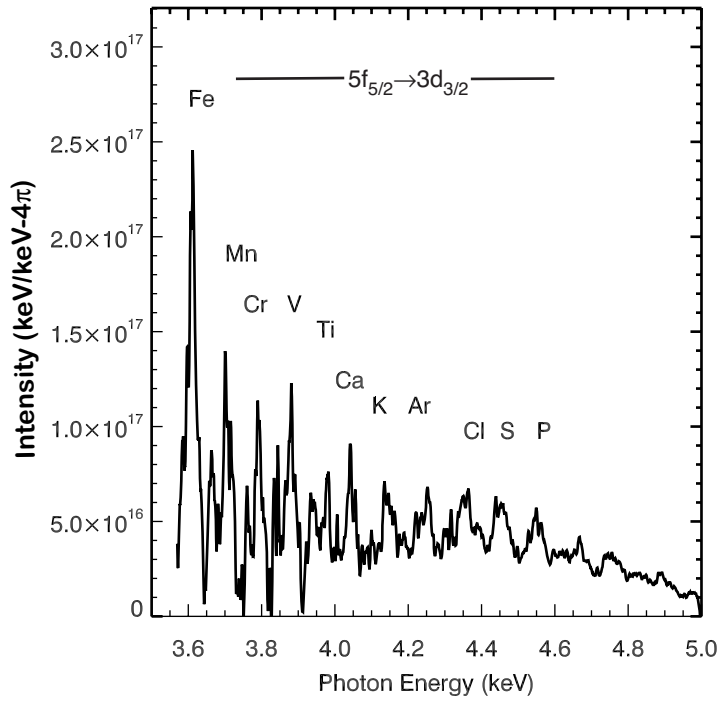


Fig. 7. Calibrated spectra from the HENWAY between 3 to 5 keV for OMEGA shot 41727.

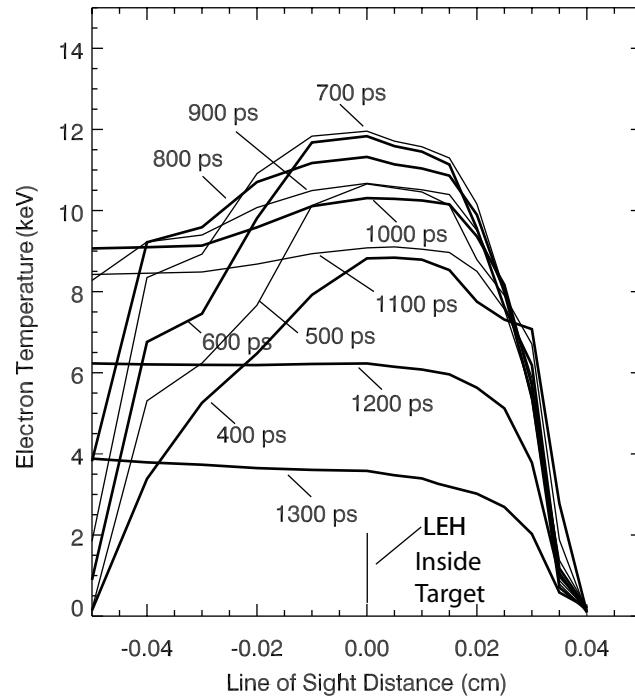


Fig. 8. Electron Temperature Simulations from LASNEX

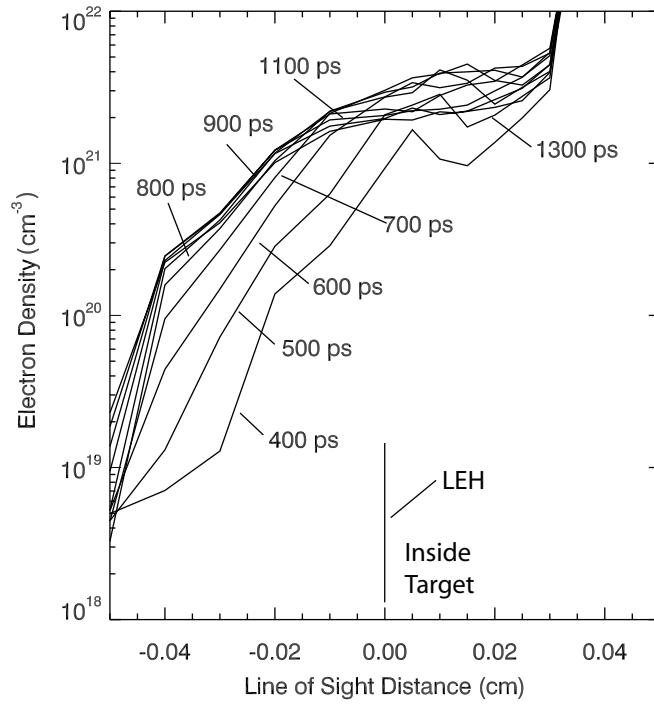


Fig. 9. Electron Density Simulations from LASNEX

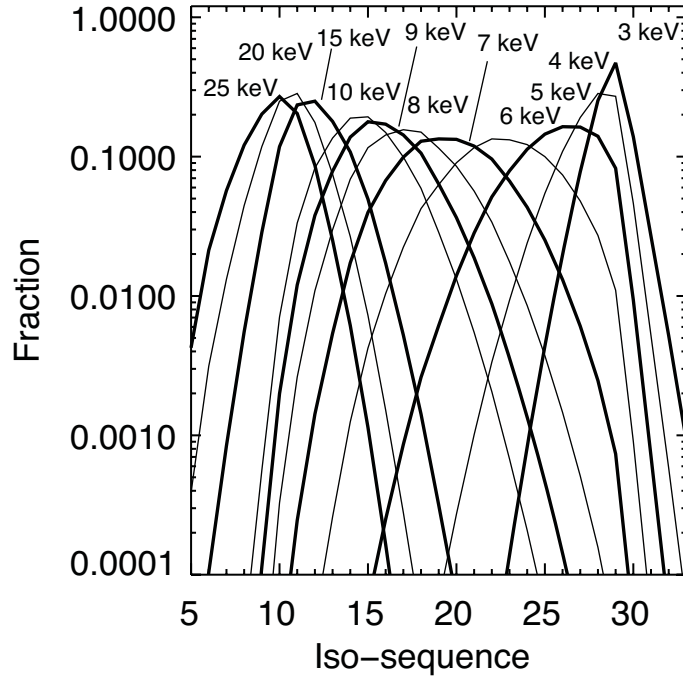


Fig. 10. Predictions for charge state distribution by FLYCHK used to simulate the HENWAY spectra. Calculations have been done at $n_e = 10^{21} \text{ cm}^{-3}$

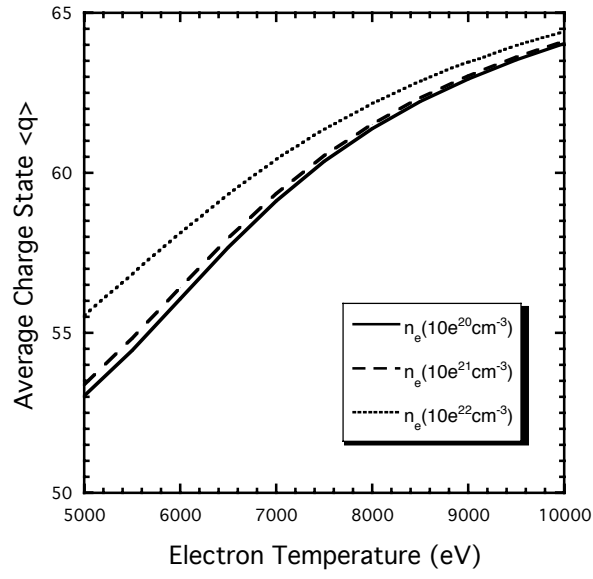


Fig. 11. Average charge state $\langle q \rangle$ predicted by FLYCHK as a function of temperature at three different electron densities.

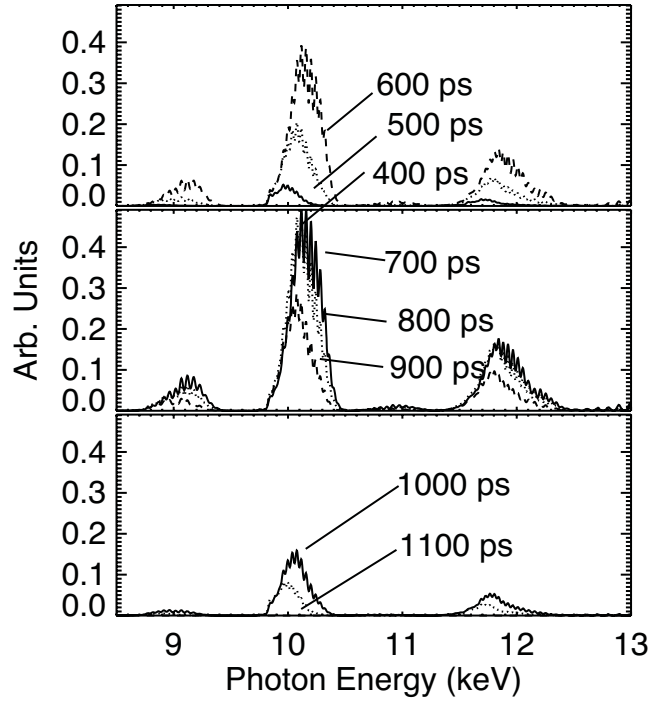


Fig. 12. Simulated spectra for photon energies from 8 to 13 keV as a function of time. The time increment is every 100 ps.

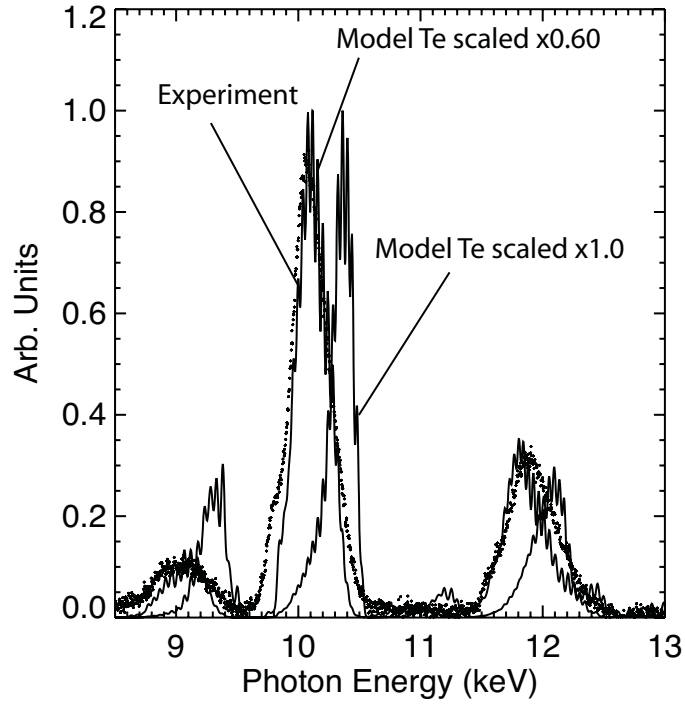


Fig. 13. Comparison of the 8 to 13 keV HENWAY spectrum and the simulations from LASNEX, FLYCHK and SCRAM/FAC. The LASNEX temperature is scaled by 1.0 and 0.65 for $n_e = 10^{21} \text{ cm}^{-3}$.

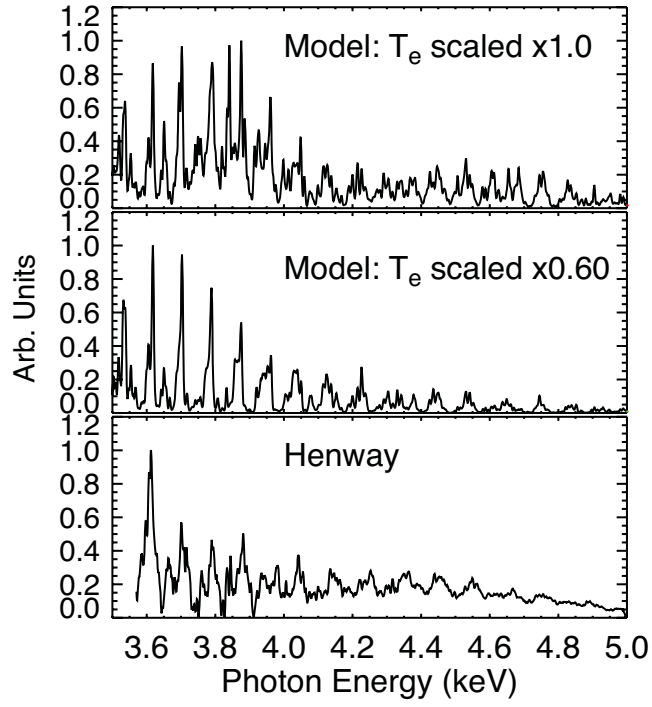


Fig. 14. Comparison of the 3 to 5 keV HENWAY spectrum and the simulations from LASNEX, FLYCHK and SCRAM/FAC. The LASNEX temperature is scaled by 1.0 and 0.65 at $n_e = 10^{21} \text{ cm}^{-3}$.

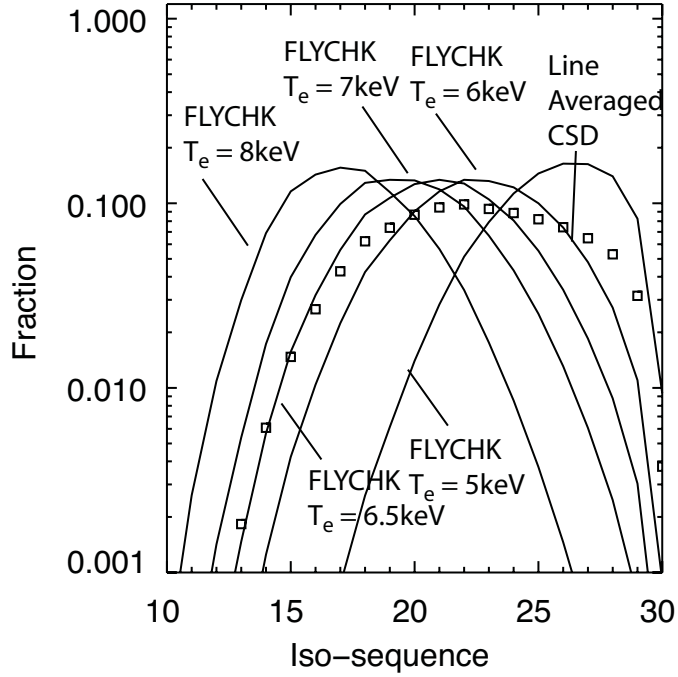


Fig. 15. Comparison of the average CSD from the HENWAY/LASNEX analysis to the predicted CSD from FLYCHK for a uniform plasma having a T_e of 6.5 keV and $n_e = 10^{21} \text{ cm}^{-3}$.